Multichiral ground states in mesoscopic *p*-wave superconductors

V. Fernández Becerra and M. V. Milošević*

Departement Fysica, Universiteit Antwerpen, Groenenborgerlaan 171, B-2020 Antwerpen, Belgium

(Received 29 July 2016; revised manuscript received 21 October 2016; published 30 November 2016)

Using Ginzburg-Landau formalism, we investigate the effect of confinement on the ground state of mesoscopic chiral p-wave superconductors in the absence of magnetic field. We reveal stable multichiral states with domain walls separating the regions with different chiralities, as well as monochiral states with spontaneous currents flowing along the edges. We show that multichiral states can exhibit identifying signatures in the spatial profile of the magnetic field if those are not screened by edge currents in the case of strong confinement. Such magnetic detection of domain walls in topological superconductors can serve as long-sought evidence of broken time-reversal symmetry. Furthermore, when applying electric current to mesoscopic p-wave samples, we found a hysteretic behavior in the current-voltage characteristic that distinguishes states with and without domain walls, thereby providing another useful hallmark for indirect confirmation of chiral p-wave superconductivity.

DOI: 10.1103/PhysRevB.94.184517

I. INTRODUCTION

In a topological superconductor besides the bulk gap that separates the normal and superconducting phases, there exist gapless edge states carrying spontaneous currents along the boundaries of the sample [1]. Theoretical works have classified the topological superconductors as two types according to whether or not they break the time-reversal symmetry (TRS), namely, (i) chiral and (ii) helical [2,3], respectively. In a chiral superconductor the Cooper pairs are spin polarized, i.e., spinless, owing to the broken TRS, and its edge states resemble those of the quantum Hall state [2]. On the other hand, in a helical superconductor the Cooper pairs are in a spin-triplet state, i.e., spinful owing to the TRS, and its edge states resemble those of the quantum spin Hall state [2].

The archetypal example of a topological superconductor breaking (satisfying) the TRS in two dimensions is the chiral (helical) p-wave model of superconductivity. In a p-wave superconductor the orbital part of the superconducting gap Δ has odd parity; that is, the Cooper pairs have angular momentum $l = 1$ since the parity P is defined by $P = -1^l$. Moreover, the spin part of the gap is either spin polarized for the chiral case or spinful with a triplet state for the helical case. Microscopic and phenomenological models of chiral p-wave superconductivity in two dimensions (2D) have reported intriguing states comprising (i) the edge states arising from the topological nature of the model [4], (ii) chiral domain walls separating regions with different chiralities [5], and (iii) coreless vortices (skyrmions) with topology and electronic properties distinctly different from that of conventional Abrikosov vortices [6–8]. However, despite the numerous works revealing the vast novel physics behind chiral p-wave superconductivity, none of the three previously mentioned hallmarks have been confirmed experimentally in strontium ruthenate (SRO) [9–12], the leading candidate to display chiral p-wave superconductivity [13].

Strontium ruthenate, Sr_2RuO_4, is a layered perovskite with a Fermi surface containing three sheets [14,15]. Among them two are one-dimensional (α and β) sheets arising from the d_{xz} and d_{yz} orbitals of Ru, whereas the remaining one is two-dimensional (γ) and arises from the d_{xy} orbitals of Ru. Chiral p-wave superconducting order was suggested to emerge in the γ band of SRO as a consequence of strong Hund's rule coupling [16]. The evidence of p-wave order in SRO to date comprises (i) the detection of spontaneous fields in muon spin resonance (μSR) experiments [17], (ii) the enhancement and suppression of the Josephson critical current depending on the direction of the junction plane [18,19], and (iii) the observation of a state breaking the TRS in the polar Kerr effect (PKE) [20]. However, measurements of the spin susceptibility below the critical temperature T_c for magnetic fields applied either parallel or perpendicular to the c axis could not demonstrate that the spins remained in the basal plane independent of the direction of the field [21,22], as one expects in chiral p-wave superconductivity. Thus, the debate about whether or not SRO is a chiral superconductor remains open, with an increasing number of works suggesting that superconducting order also develops in α and β bands and that they play an essential role in the physical properties of this material [23–26].

In this work we employ the phenomenological Ginzburg-Landau (GL) model to describe chiral p-wave superconductors [27]. The set of coupled and nonlinear differential equations that we solve numerically for the two-component superconducting order parameter, $\vec{\Psi} = (\psi_+, \psi_-)^T$, and the vector potential $\vec{A}$ depends on four phenomenological parameters, defined by the shape of the Fermi surface of the material under consideration [4,28]. We then use the microscopic information available for SRO to calculate the four phenomenological parameters and present striking results useful to explain the elusive detection of chiral domain walls (DWs). From our simulations we present the ground-state phase diagram as a function of the size and aspect ratio of the mesoscopic p-wave superconducting samples in the absence of any applied magnetic field. Among the stable phases, we reveal the multichiral states with domain walls separating the regions with different chiralities, as well as monochiral ones with spontaneous currents flowing along the edges. Finally, we report the characteristic features of the chiral domain walls that can be directly detected in magnetic and transport measurements.

*milorad.milosevic@uantwerpen.be

 ©2016 American Physical Society

This paper is organized as follows. Section II presents the theoretical formalism and the discussion of the gauge invariance in the GL equations. From there we derive the equations that describe the considered system, namely, mesoscopic rectangular samples with and without an external magnetic field and nanobridges with normal leads where an external current is applied. Section III then discusses our findings in a phase diagram of ground states, showing the stability and relationship between the superconducting configurations composed of multiple chiral domains as well as the monochiral states. For the nanobridges the current-voltage characteristics are analyzed in Sec. IV as a function of sample size and external magnetic field, with reported features that distinguish states with and without domain walls. Our findings and conclusions are summarized in Sec. V.

II. THEORETICAL FORMALISM

Based on the point symmetry of the crystal structure under consideration, one can obtain the GL functional and, subsequently by its minimization, the time-dependent Ginzburg-Landau (TDGL) equations, which describe the spatial distribution of the magnetic induction $\vec{B}$ and the superconducting order parameter $\vec{\Psi}$. Within an analysis for unconventional superconductivity, a GL functional with a state breaking the TRS of the p-wave type has already been reported for a tetragonal lattice [27]. Thus, the dimensionless GL functional, $\mathscr{F} = \mathscr{F}'/\mathscr{F}_0$, where $\mathscr{F}_0 = \hbar^2\Delta_0^2/2m\xi^2$, for chiral p-wave superconductors reads

$$\begin{aligned}\mathscr{F} = &\frac{K+k_1}{4}(|\vec{D}\,\psi_+|^2 + |\vec{D}\,\psi_-|^2)\\ &+(k_2+k_3)\mathrm{Re}\{\Pi_+\psi_-(\Pi_-\psi_+)^*\}\\ &-\frac{1}{2}|\vec{\Psi}|^2+\frac{1+\tau}{8}|\vec{\Psi}|^4-\frac{\tau}{8}(\vec{\Psi}^*\hat{\sigma}_z\vec{\Psi})^2\,, \end{aligned} \tag{1}$$

where $\xi = \sqrt{\frac{\hbar^2}{2m\alpha}}$ is the superconducting coherence length and $\Delta_0 = \sqrt{\frac{\alpha}{2\beta_1}}$ is the magnitude of the degenerate zero-field solution, $\vec{\eta}_0 = \Delta_0(1,\pm i)/\sqrt{2}$, in the fields $\eta_x = (\psi_- + \psi_-)/2$ and $\eta_y = (\psi_+ - \psi_-)/2i$. In Eq. (1), k_i, α, and $\tau = \beta_2/\beta_1$, with $i = 1,2,3$, are parameters microscopically derived depending on the Fermi surface of the material. For SRO Refs. [4,28] give a detailed calculation of these parameters assuming chiral superconductivity develops in the cylindrical γ band. $K = \sum k_i$, $\vec{D}$ is the covariant derivative, and $\Pi_\pm = \frac{1}{\sqrt{2}}(D_x \pm i D_y)$ are creation and annihilation operators of Landau levels, respectively. In dimensionless units where time is scaled to the GL time $t_0 = \xi^2/D$, with D being a diffusion phenomenological coefficient, the distance to the coherence length ξ, the magnetic field to the upper critical field H_{c2}, and the electrostatic potential to $\varphi_0 = H_{c2}\xi^2/ct_0$, where c is the speed of light, the TDGL equations become [29,30]

$$\left(\frac{\partial}{\partial t} + i\varphi\right)\vec{\Psi} = -\frac{\delta\mathscr{F}}{\delta\vec{\Psi}^*}, \tag{2}$$

$$\sigma\left(\frac{\partial\vec{A}}{\partial t} + \vec{\nabla}\varphi\right) = -\frac{\delta\mathscr{F}}{\delta\vec{A}} - \kappa^2\vec{\nabla}\times\vec{B}\,. \tag{3}$$

In Eqs. (2) and (3) $\vec{B}$ is the magnetic induction, φ is the electrostatic potential, σ is the conductivity in units of $D/\alpha t_0$, and $\kappa = \lambda/\xi$ is the GL parameter, where $\lambda = \sqrt{\frac{mc^2}{8\pi e^2\Delta_0^2}}$ is the London penetration depth.

The gauge invariance of the TDGL equations allows one to simplify them owing to the freedom of the arbitrary function χ in the transformation $(\vec{\Psi}',\vec{A}',\varphi') = (\vec{\Psi}e^{i\chi},\vec{A}+\nabla\chi,\varphi - \frac{\partial\chi}{\partial t})$. When χ is properly chosen (gauge fixed), it provides a supplementary equation for the transformed fields that simplifies the form of the TDGL equations. In what follows we present the two gauge choices considered in this work.

A. Zero-electrostatic-potential gauge

The zero-electrostatic-potential gauge is the most convenient choice for the TDGL equations when neither charges nor external currents are considered in the superconducting sample [7]. From the original fields $(\vec{\Psi},\vec{A},\varphi)$ the arbitrary function χ is required to satisfy the equation $\frac{\partial\chi}{\partial t} = \varphi$. This choice renders vanishing the transformed electrostatic potential, $\varphi' = 0$, reducing considerably the complexity of the TDGL equations for the transformed fields,

$$\begin{aligned}\frac{\partial\vec{\Psi}}{\partial t} = &\left(\frac{K+k_1}{2}\vec{D}^2 + (k_2+k_3)[\Pi_+^2\hat{\sigma}_+ + \Pi_-^2\hat{\sigma}_-]\right)\vec{\Psi}\\ &+\left(1 - \frac{1+\tau}{2}|\vec{\Psi}|^2 \pm \frac{\tau}{2}\vec{\Psi}^*\hat{\sigma}_z\vec{\Psi}\right)\vec{\Psi}, \end{aligned} \tag{4}$$

$$\sigma\frac{\partial\vec{A}}{\partial t} = \vec{J} - \kappa^2\vec{\nabla}\times\vec{B}, \tag{5}$$

where for convenience we have dropped all the primes and $\hat{\sigma}_\pm = (\hat{\sigma}_x \pm i\hat{\sigma}_y)/2$ are pseudospin or chiral operators acting on the space span by $\psi_\pm$. It is straightforward to show in Eq. (4) that by considering (i) the stationary regime, i.e., $\frac{\partial\vec{\Psi}}{\partial t} = 0$, and (ii) the proximity of the superconducting to the normal phase, i.e., discarding the nonlinear terms, the first GL equation transforms to the eigenvalue problem: $[\frac{K+k_1}{2}\vec{D}^2 + (k_2+k_3)(\Pi_+^2\hat{\sigma}_+ + \Pi_-^2\hat{\sigma}_-)]\vec{\Psi} = -\vec{\Psi}$. The analytical solutions to the latter equation have been obtained from Landau level states ϕ_n satisfying the equations $\Pi_\pm\phi_n \propto \phi_{n\pm1}$ [27,28,31]. Thus, in the linearized case for chiral p-wave superconductors the order parameter is given by $\vec{\Psi} = (\phi_n,\phi_{n-2})^T$, where n becomes the vorticity.

Finally, with $\{\hat{\imath},\hat{\jmath}\}$ being canonical base vectors in Cartesian coordinates, the dimensionless superconducting density current $\vec{J}$, given in units of $J_0 = \frac{e\hbar}{m\xi}\Delta_0^2$, reads

$$\begin{aligned}\vec{J} = \mathrm{Im}\Big\{&\frac{K+k_1}{4}(\psi_+^*\vec{D}\psi_+ + \psi_-^*\vec{D}\psi_-) + \frac{k_2+k_3}{2\sqrt{2}}(\vec{\Psi}^*[\Pi_+\hat{\sigma}_+\\ &+\Pi_-\hat{\sigma}_-]\vec{\Psi}\,\hat{\imath} + i\,\vec{\Psi}^*[\Pi_+\hat{\sigma}_+ - \Pi_-\hat{\sigma}_-]\vec{\Psi}\,\hat{\jmath})\Big\}. \end{aligned} \tag{6}$$

B. Coulomb gauge

The Coulomb gauge, unlike the zero-electrostatic-potential gauge, is the most convenient choice when an external current is applied to the superconducting sample [32,33]. In this case the arbitrary function is required to satisfy the equation $\Delta\chi =$

$-\vec{\nabla}\cdot\vec{A}$, which makes the transformed vector potential $\vec{A}'$ divergence free at all times. Then, after taking the divergence of Eq. (3) and dropping all the primes, the TDGL equations become

$$\left(\frac{\partial}{\partial t}+i\varphi\right)\vec{\Psi}=\left(\frac{K+k_1}{2}\vec{D}^2+(k_2+k_3)[\Pi_+^2\hat{\sigma}_+ +\Pi_-^2\hat{\sigma}_-]\right)\vec{\Psi}$$
$$+\left(1-\frac{1+\tau}{2}|\vec{\Psi}|^2\pm\frac{\tau}{2}\vec{\Psi}^*\hat{\sigma}_z\vec{\Psi}\right)\vec{\Psi} \quad (7)$$

and

$$\sigma\Delta\varphi=\vec{\nabla}\cdot\vec{J}\,. \quad (8)$$

It is noteworthy that the second TDGL equation is for the electrostatic potential rather than the vector potential as in Eq. (5). The vector potential in this case is obtained from the gauge choice $\vec{\nabla}\cdot\vec{A}=0$.

C. Boundary conditions

Equations (4) and (5) are solved in this work for mesoscopic rectangular samples with an external magnetic field H applied perpendicularly to the sample plane. The required boundary conditions that pose the problem well and that are compatible with the existence of spontaneous edge currents are [4,7,27]

$$\left.\begin{aligned}\psi_+-\psi_-&=0\\ D_y\psi_+ + D_y\psi_-&=0\end{aligned}\right\}\ \text{at the north and south sides,}$$

$$\left.\begin{aligned}\psi_+ +\psi_-&=0\\ D_x\psi_+ - D_x\psi_-&=0\end{aligned}\right\}\ \text{at the east and west sides,}$$

$$(\nabla\times\vec{A})\cdot\hat{n}=H, \quad (9)$$

where $\hat{n}$ is the unitary vector normal to the sample surface. On the other hand, Eqs. (7) and (8) are solved in this work for nanobridges linking two normal leads, which are located at the north and south sides and are used to apply current to the superconducting sample. The corresponding boundary conditions for the fields $(\vec{\Psi},\varphi)$ are therefore

$$\left.\begin{aligned}\psi_\pm&=0\\ \partial_y\varphi+j_n&=0\end{aligned}\right\}\ \text{at the north and south sides,}$$

$$\left.\begin{aligned}\psi_+ +\psi_-&=0\\ D_x\psi_+ - D_x\psi_-&=0\\ \partial_x\varphi&=0\end{aligned}\right\}\ \text{at the east and west sides.} \quad (10)$$

The sets of equations (4) and (5) and (7) and (8) are numerically solved using finite differences and the link variables technique of Refs. [29,34] with the corresponding boundary conditions (9) and (10), respectively.

Before concluding this section, we give the reduced (hence more convenient) expression for the dimensionless free-energy density, obtained by transformation of Eq. (1):

$$\frac{f}{f_0}=-\frac{1}{V}\int dV\left\{\frac{1+\tau}{8}|\vec{\Psi}|^4-\frac{\tau}{8}(\vec{\Psi}^*\hat{\sigma}_z\vec{\Psi})^2-\kappa^2\vec{B}^2\right\}. \quad (11)$$

The energetic considerations enable us to find not only the lowest-energy (ground) states but also other stable states with higher energies (metastable states).

III. GROUND-STATE PHASE DIAGRAM

In this section we solve the TDGL equations using the zero-electrostatic-potential gauge for rectangular $w_x\times w_y$ mesoscopic samples with sizes in the range $[3.5\xi,23\xi]$. We consider no external magnetic field and obtain the superconducting ground states according to the following procedure. (i) For the chosen size of the sample we numerically solve Eqs. (4) and (5) with different initial inputs, e.g., one domain wall (DW) at the half width of the sample,

$$\vec{\Psi}=\begin{pmatrix}1\\0\end{pmatrix}\ 0\leqslant x\leqslant 0.5\,w_x,\quad \vec{\Psi}=\begin{pmatrix}0\\1\end{pmatrix}\ 0.5w_x<x\leqslant w_x.$$

Other initial inputs in the set have two, three, and four DWs distributed in the sample either horizontally or vertically. Moreover, initial inputs without DWs are considered as well, such as $\vec{\Psi}=(1,0)^T$ and $\vec{\Psi}=(0,1)^T$ throughout the sample. (ii) After the numerical simulations using different initial inputs, we compare the energies of all found solutions, using Eq. (11), and identify the lowest-energy solution. (iii) The process is repeated for all the samples with sizes in the range $w_x,w_y\in[3.5\xi,23\xi]$.

Figure 1 shows the phase diagram of the ground state at zero external magnetic field for mesoscopic rectangular samples of different sizes. For the phenomenological parameters, microscopic calculations have demonstrated that $k_1=k_2=k_3=1/3$ and $\tau=1/2$ for chiral superconductivity developing in a cylindrical Fermi surface [4,28]. The two remaining parameters (κ and σ) are taken as 1.25 and 1, respectively. The value of κ was chosen to weakly deviate from the in-plane bulk GL parameter κ_{ab} of SRO [14,15] in order to compare our results with previously reported works based on the BCS model for chiral p-wave superconductivity [4]. The value of σ was set to 1 as typically used [29,30]. This

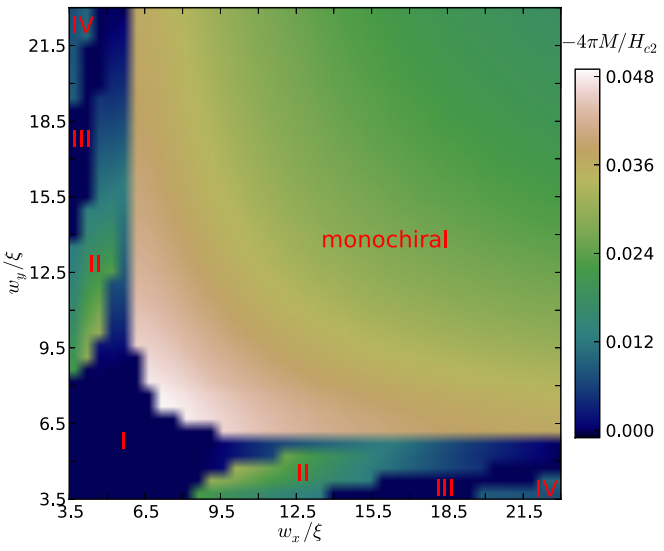

FIG. 1. The phase diagram of the ground state of rectangular p-wave samples in the absence of external magnetic field. Five different phases (one monochiral and four multichiral) are clearly distinguished and exhibit distinct magnetic responses. The multichiral phases are labeled I-IV according to the number of domain walls they contain. The monochiral state is free of domain walls.

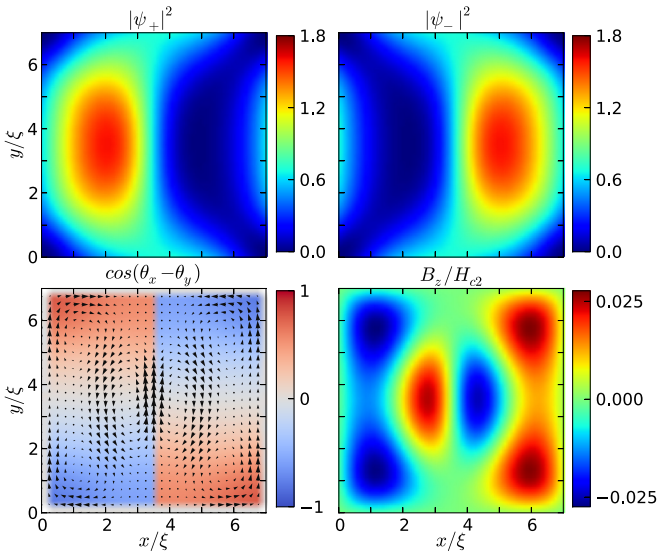

FIG. 2. Contour plots of the superconducting density components $|\psi_\pm|^2$, the phase difference $\cos(\theta_x - \theta_y)$, and the magnetic induction B_z of a ground state with one domain wall. $\theta_{x,y}$ are the angular phases of $\eta_{x,y}$, where $\eta_x = (\psi_+ + \psi_-)/2$ and $\eta_y = (\psi_+ - \psi_-)/2i$. The spatial distribution of the superconducting current density $\vec{J}$ is superimposed on the contour plot of $\cos(\theta_x - \theta_y)$.

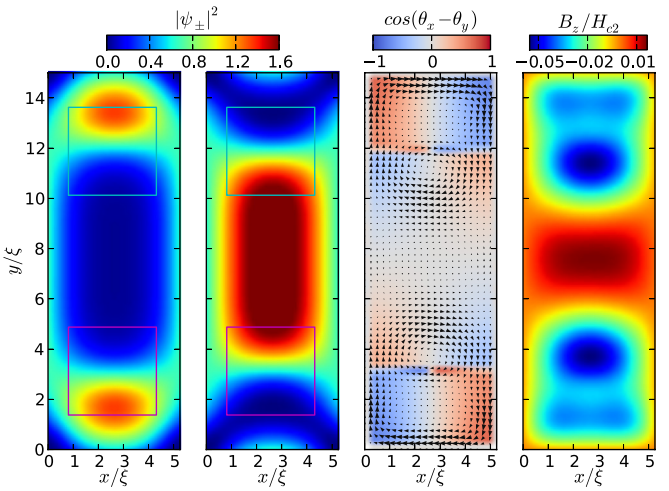

FIG. 3. Same quantities as in Fig. 2 but for a ground state with two domain walls. The two pairs of boxes with different colors are displayed in order to highlight the regions where the shape of the sample strongly affects the order parameter components and breaks the mirror symmetry of the domain wall. Consequently, only one quasicircular clockwise stream of current is preserved in the vicinity of the domain walls, while the anticlockwise current on the other side of the wall (see Fig. 2) is annihilated by the currents stemming from the sample edges.

choice has weak implications for the stationary solution of Eqs. (4) and (5), as it predominantly influences the dynamical regime by determining the distribution of the electrostatic potential in the presence of applied current. The diagram shows five different phases, distinguished according to their magnetization. Multichiral phases are denoted by Roman numerals according to the number of domains walls they contain. Monochiral phase is free of DWs.

Figure 2 shows a superconducting state belonging to phase I of the diagram in Fig. 1, i.e., a state with one domain wall, as seen in the contour plots of $|\psi_\pm|^2$. Note that the two-component order parameter $\vec{\Psi}$ can also be expressed in terms of its Cartesian components η_x and η_y (as $\eta_x = \frac{\psi_+ + \psi_-}{2}$ and $\eta_y = \frac{\psi_+ - \psi_-}{2i}$), whose phases θ_x and θ_y can be employed for better identification of topological defects in p-wave superconductors (see Ref. [7]). The quantity $\cos(\theta_x - \theta_y)$, from now on simply called the phase difference, conveniently indicates the exact position of the DWs (the interface separating the regions where the chirality is dominated by ψ_+ on one side and by ψ_- on the other side). The spatial distribution of the superconducting current density $\vec{J}$ [see Eq. (6)] is also plotted in Fig. 2. It is superimposed on the contour plot of the phase difference, and it shows (i) the currents of the DW flowing from the south to the north side and (ii) the spontaneous currents of the edge states flowing clockwise and counterclockwise on the west and east sides of the sample, respectively. Consequently, the contour plot of the magnetic induction B_z shows (i) the typical dipole profile expected from a DW at the sample center and (ii) the magnetic induction arising from the spontaneous currents on the left and right sides [4,5,7]. It is noteworthy that by slightly increasing the ratio between the sample height w_y and width w_x, one can shift the vertical position of the DW. This fact leads us to the discussion of the following states.

Changing the aspect ratio $r = w_y/w_x$ from 1, phase II becomes the ground state. We show in Fig. 3 one of the ground states belonging to this phase. It exhibits in the contour plots of $|\psi_\pm|^2$ and $\cos(\theta_x - \theta_y)$ two horizontal DWs located close to the north and south sides of the sample. However, the contour plot of the magnetic induction, which is expected to show characteristic dipolelike profiles at each DW, does not show any clear signature of DWs. This is caused by

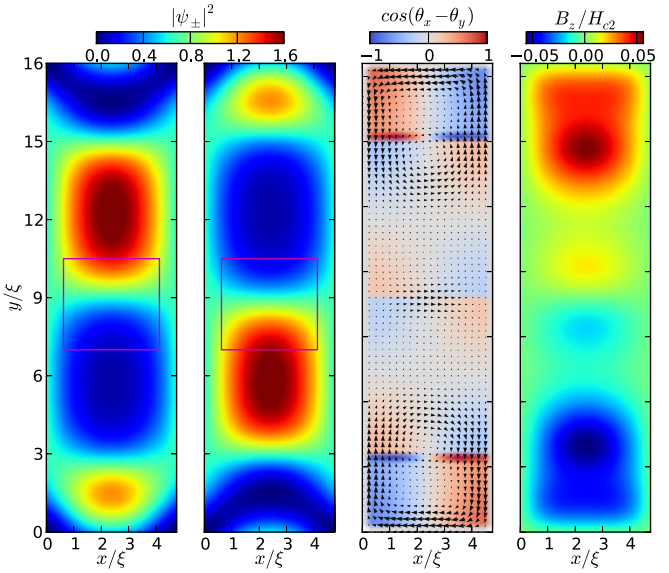

FIG. 4. Same quantities as in Fig. 2 but for a state with three domain walls. A pair of boxes is displayed in order to highlight the local symmetry existing between the components, $|\psi_+|^2$ and $|\psi_-|^2$, related to the current distribution in the vicinity of the domain walls.

(i) the vorticity of this state ($\nu_+ = 0$ and $\nu_- = -2$) and (ii) the shape of the superconducting sample (rectangular), which causes the two DWs to reside close to the north and south sides of the sample. As a consequence, the current on one side of the DW interacts (annihilates) with the edge current, which diminishes the magnetic response on that side and the characteristic dipolar signature is lost.

When making the aspect ratio r of the sample more acute, one obtains as the ground state three DWs, i.e., phase III. In Fig. 4 we show a state belonging to this phase. Again, the contour plot of the magnetic induction confirms that top and bottom DWs do not show their characteristic dipole profiles, whereas the central DW does. The dipole profile on the central DW is maintained because of its weak interaction with the edge currents, so that the local symmetry between the two components $|\psi_+|^2$ and $|\psi_-|^2$ is maintained (see the regions enclosed by boxes in Fig. 4).

In the ground-state phase diagram of Fig. 1, the phase containing four DWs is obtained only for extreme aspect ratios of the sample ($r > 5$). One state belonging to this phase is shown in Fig. 5 for a narrow sample with $w_x = 4\xi$. According to the contour plot of the phase difference, the four DWs appear almost equidistantly distributed along the sample. However, the typical magnetic responses for the DWs expected in the contour plot of the magnetic induction are absent. The reason for this behavior is the imbalance between the superconducting components $|\psi_+|^2$ and $|\psi_-|^2$, which one can clearly see in the line profiles along $x = 2\xi$, shown in Fig. 5(b). Namely, the strong confinement in the x direction has a stronger influence on ψ_+ than on ψ_-, which affects the balance between the two components required for the formation of the DW currents and consequently diminishes the dipolar profile of the DW in the magnetic induction.

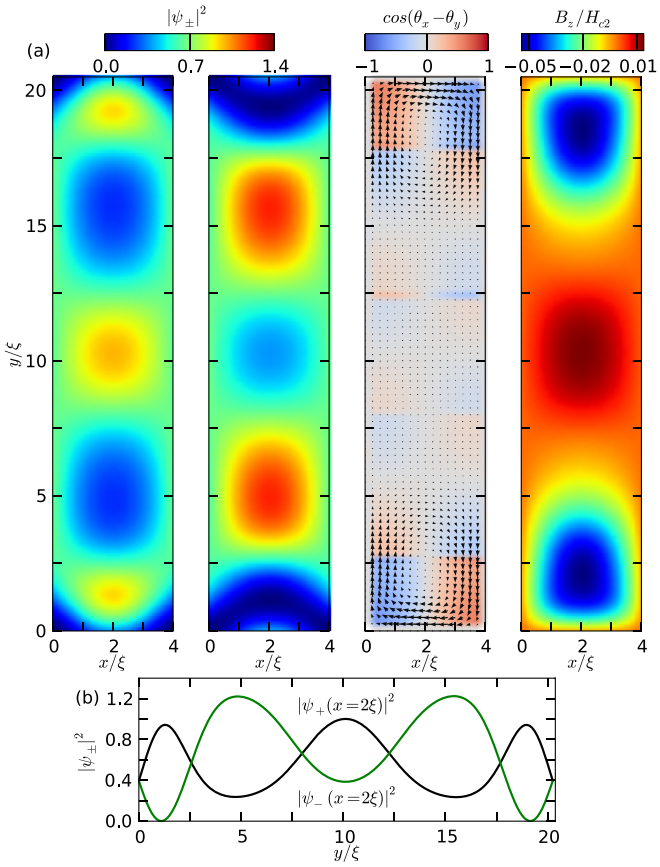

FIG. 5. (a) The same quantities as in Fig. 2 but for a state with four domain walls. (b) The line profiles of the superconducting density components $|\psi_\pm|^2$ along the line defined by $x = 2\xi$.

Finally, in what follows we discuss the phase that is free of DWs, i.e., the monochiral phase. It is the most present phase in the diagram of Fig. 1, as it spans samples ranging from size $(w_x \times w_y) = (7\xi \times 7\xi)$ up to $(23\xi \times 23\xi)$. Based on the transformation of dimensionless units to real units [using the temperature dependence of the coherence length $\xi = \xi(0)/\sqrt{1 - T/T_c}$, choosing $\xi(0)$ to fit SRO and $T = 0.95T_c$], the ground state of a p-wave superconducting sample with size $20\xi \times 20\xi$ (approximately 6×6 μm) will be free of DWs in the ground state. However, this does not mean that the magnetic response of the ground states belonging to the monochiral phase is negligible. On the contrary, the contour plot of the magnetic induction in Fig. 6(a) shows a significant magnetic response of this monochiral state, with spontaneous currents flowing along the edges. The characteristic scale for the magnetic response of the spontaneous currents is $\zeta = 1.6875\xi$, slightly different from the natural scale for the magnetic induction $\lambda = 1.25\xi$, presumably due to weak confinement effects. Then, in order to describe further the effects of confinement on the ground state in the monochiral phase, Fig. 6(b) shows line profiles of the magnetic induction of square samples with sizes 10ξ, 13ξ, 16ξ, 19ξ, and 22ξ. Here one can notice that owing to the confinement, the left and right edge currents interact strongly in the square samples

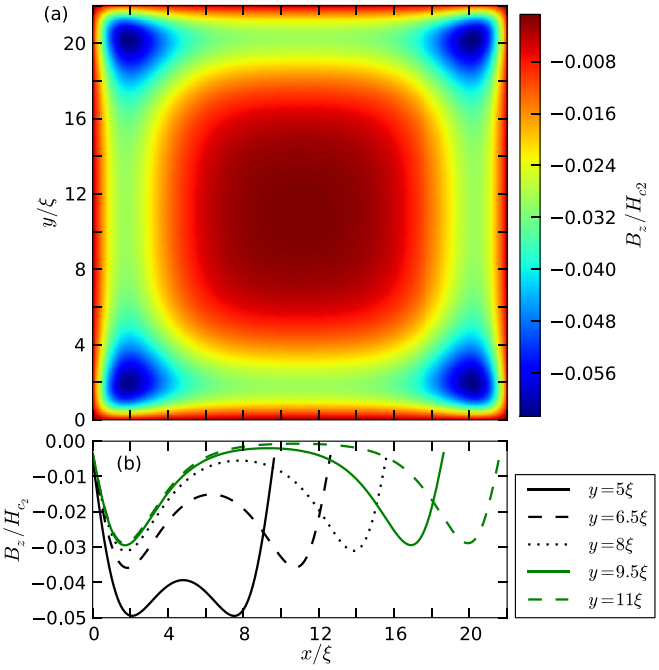

FIG. 6. (a) Magnetic induction of a square sample with dimensions $(22\xi \times 22\xi)$ at zero external magnetic field. The spontaneous currents flowing clockwise give rise to the negative values of B_z. (b) Line profiles of the magnetic induction of different square samples along the central cut through the sample.

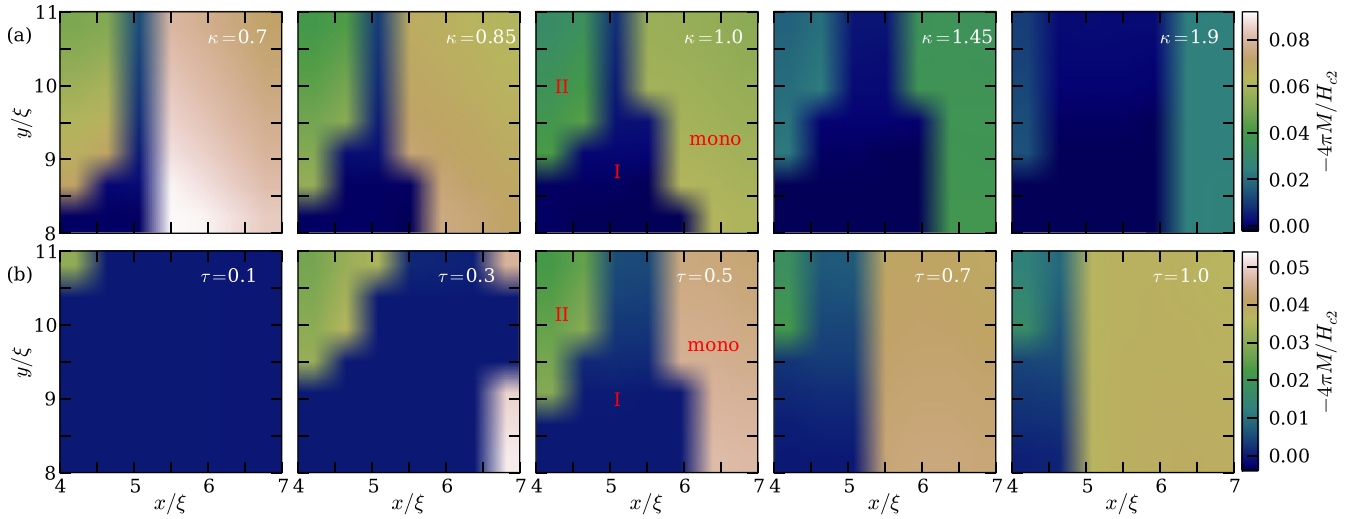

FIG. 7. Diagram of ground states for different values of the phenomenological parameters κ and τ. The color scales indicate the corresponding magnetization of the ground states. The panels show the part of the phase diagram containing the monochiral phase and the multichiral phases I, II, and demonstrate the influence that the parameters have on these phases.

smaller than $19\xi \times 19\xi$; that is, in the central region of the sample the value of the magnetic induction becomes notably nonzero below a certain sample size due to the overlap and interaction of spontaneous currents stemming from opposite edges of the sample.

A. Influence of the parameters on the ground-state phase diagram

The phase diagram shown in Fig. 1 was obtained for the phenomenological parameters adjusted to represent a chiral p-wave superconductor with a cylindrical Fermi surface (presumably SRO falls in this category). However, the fact that the spontaneous currents in SRO have remained elusive so far questions the emergence of chiral order in this material. Large efforts have been made to reconcile the experiments with theory, including works analyzing the effect of disorder on the spontaneous currents [35,36], as well as the possibility of chiral non-p-wave order in SRO [37].

Recent works have also considered that superconductivity can develop in the other two bands of SRO (α and β) [23–26]. Surprisingly, in this scenario of multiband superconductivity one of the predictions is that the spontaneous currents are strongly suppressed owing to the existence of the α and β bands. Quantitatively, the suppression is due to a considerable reduction of the k_2 and k_3 parameters [26] [see in Eq. (6) that the term that supports the chiral currents is multiplied by the sum of k_2 and k_3]. The effect of such changed values of k_i, i.e., $k_i \neq 1/3$, on the superconducting states of mesoscopic samples has already been discussed elsewhere [6,7]. However, little is known about the robustness of multichiral states against the variation of parameters κ and τ. In Fig. 7 we focus on one part of the phase diagram to illustrate the influence that these parameters have on the transitions between the monochiral and the multichiral (I,II) states and then draw generic conclusions. As a first important finding, one can see in the sequence of Fig. 7(a) that the phase with the multichiral state of Fig. 2 expands as κ is increased; that is, the magnetic response of the sample is disfavored. The expansion of phase I occurs at the expense of the phase II and the monochiral phase since they become less favorable owing to their nonzero magnetization.

To understand the influence of the parameter τ on the phases of Fig. 7 before looking at the actual results, one can analyze the condensation energy of Eq. (1) (the last three terms) to gain insight into the expected behavior. The minima of $\mathscr{F}_{\rm cond} = -\frac{1}{2}|\vec{\Psi}|^2 + \frac{1+\tau}{8}|\vec{\Psi}|^4 - \frac{\tau}{8}(\vec{\Psi}^*\hat{\sigma}_z\vec{\Psi})^2$ are the degenerate states: $(|\psi_+| = \sqrt{2},\ \psi_- = 0)$ and $(\psi_+ = 0,\ |\psi_-| = \sqrt{2})$. These states are separated by a barrier which is proportional to τ. One can obtain the shape of this barrier by replacing $|\psi_+| = \sqrt{2}\cos\theta$ and $|\psi_-| = \sqrt{2}\sin\theta$, so the condensation energy expression becomes $[\mathscr{F}_{\rm cond} = \frac{\tau-1}{2} - \frac{\tau}{4}\cos^2(2\theta)]$. One should notice that the barrier disappears when $\tau = 0$, leading to the removal of the degeneracy of the ground state. That means that one should not expect the formation of domain walls if τ is close to zero. However, in the sequence of Fig. 7(b) one sees that phase I is the most dominant one at $\tau = 0.1$. The reason for this seemingly counterintuitive result is that the last term of $\mathscr{F}_{\rm cond}$ is not the only one that breaks TRS. In fact, the second term in the kinetic energy of Eq. (1) also breaks TRS, and in this case is the term that favors the multichiral over the monochiral states.

From Fig. 7(b) one can also deduce that the effect on phase I of increasing τ is the opposite of increasing κ. As τ is increased, phases I and II give way to the expansion of phase V. This effect can be attributed to the increase of the barrier separating the degenerate ground states. When the barrier is high such that the spatial fluctuations (real or, in our case, numerical) cannot overcome it, the combination of degenerate states becomes energetically unfavorable, leading the system to prefer the monochiral state.

IV. TRANSPORT SIGNATURES OF DOMAIN WALLS IN MULTICHIRAL STATES

In this section we solve the TDGL equations using the Coulomb gauge for nanobridges with normal leads at the

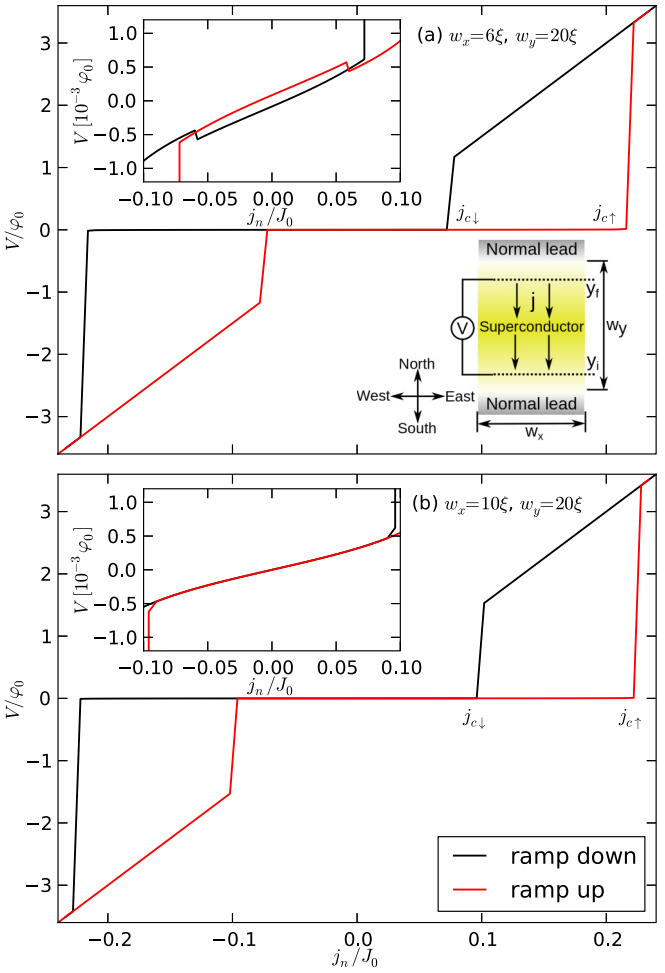

FIG. 8. The voltage as a function of the applied current density for two nanobridges of the same length ($w_y = 20\xi$) with different widths: (a) $w_x = 6\xi$ and (b) $w_x = 10\xi$ (b). The bottom inset in (a) shows the nanobridge, along with the normal leads used to apply the current, and the points where the voltage is measured, namely, $y_f = 17.5\xi$ and $y_i = 2.5\xi$. The top inset in (a) and the inset in (b) show the opening and the absence, respectively, of the hysteretic loop of the voltage vs current density in the superconducting phase, i.e., the phase with nearly zero voltage drop.

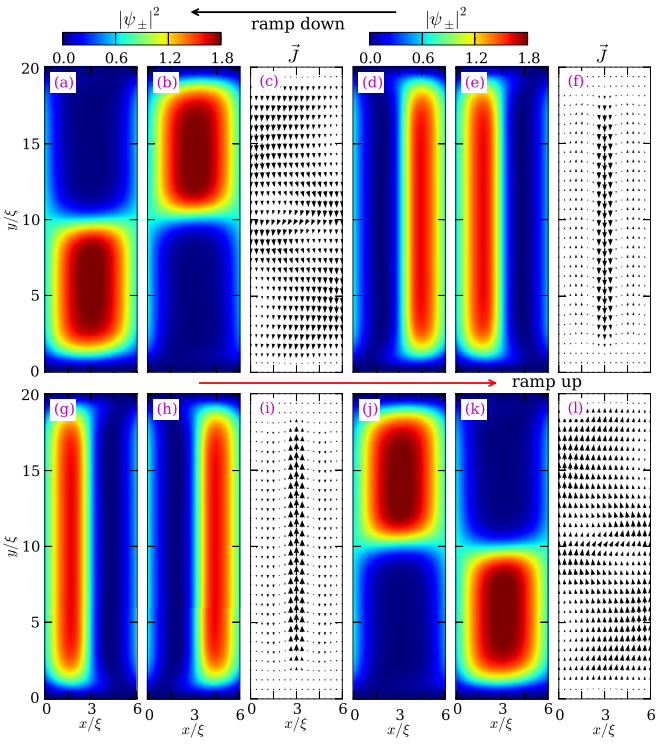

FIG. 9. Four representative states during (a)–(f) the ramp down and (g)–(l) ramp up of the current in the V vs j plot of Fig. 8(a). The quantities shown are the contour plots of the superconducting order parameters $|\psi_\pm|^2$ and the vectorial flow of the current density $\vec{J}$.

north and south sides [see the bottom inset of Fig. 8(a)]. These leads are used to apply an external current density j_n to the superconducting sample in order to measure the voltage drop between two voltage contacts, namely, y_i and y_f. In dimensionless units and at zero external magnetic field, the voltage versus the current density (j_n-V characteristic) is plotted in Fig. 8 for two nanobridges of length 20ξ and widths 6ξ [Fig. 8(a)] and 10ξ [Fig. 8(b)]. The obtained j_n-V characteristics are apparently similar, with two different critical currents for $j_n > 0$ ($j_{c\downarrow} < j_{c\uparrow}$) depending on whether j_n is decreased (ramped down) or increased (ramped up). However, a close-up of the superconducting phase, i.e., the phase with nearly zero measured voltage, shows a distinctly different behavior, as seen in the top inset in Fig. 8(a) and the inset in Fig. 8(b). The hysteretic loop in the superconducting phase opens in Fig. 8(a) but is absent in Fig. 8(b). In order to understand the origin of the hysteresis within the superconducting phase, in what follows we describe the order parameters that correspond to these cases.

Figure 9 directly shows the superconducting states responsible for the opening of the hysteretic loop in the j_n-V characteristic of Fig. 8(a). The top row in Fig. 9 shows two representative states corresponding to the ramp down of j_n, whereas the bottom row shows two representative states corresponding to the ramp up of j_n. From the top (bottom) row one can easily see that by ramping down (ramping up) the current from the normal phase, one vertical DW with chiral currents flowing downward (upward) is formed. Subsequently, as the external current is further decreased (increased), the vertical DW transforms to a horizontal DW with leftward (rightward) currents. Furthermore, one can also notice that the states with vertical DWs, as well as the states with horizontal DWs, form the pair of degenerate states owing to the broken TRS. That means that under the transformation $|\psi_+|_d \rightarrow |\psi_-|_h$ and $|\psi_-|_e \rightarrow |\psi_+|_g$, the reduced expression of the free energy [Eq. (11)] remains unchanged. Thus, we claim that the combination of degenerate superconducting states with opposite currents (vertical DWs) and the fact that the voltage in the nanobridge is measured transversally to them lead to the hysteretic behavior seen in the inset of Fig. 8(a).

However, when the width of the nanobridge is changed, e.g., to $w = 10\xi$, the degenerate states become monochiral, allowing the formation of spontaneous currents flowing along the edges of the sample for each case but with opposite directions [clockwise as in Fig. 10(c) and counterclockwise as in Fig. 10(f)]. The corresponding voltage drop, reported in

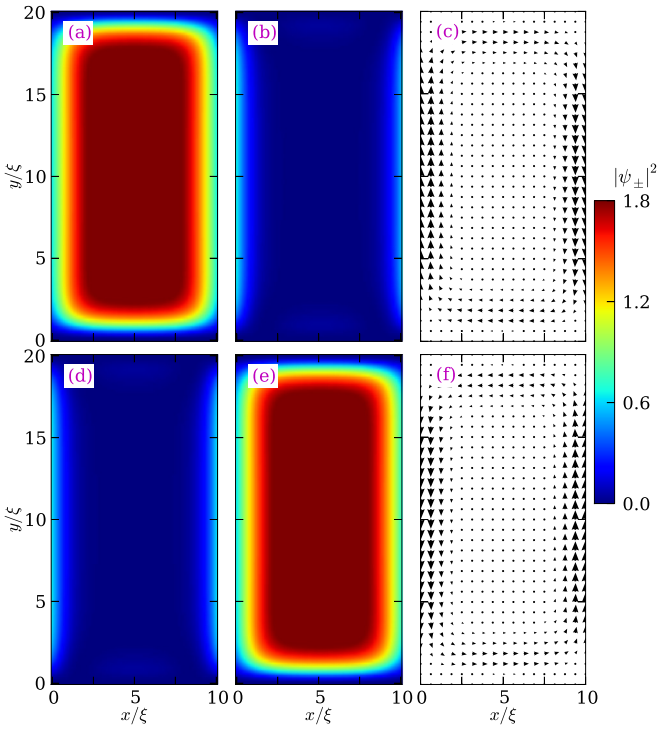

FIG. 10. Same quantities as in Fig. 9 but for the states in the superconducting phase for (a)–(c) the ramp down and (d)–(f) ramp up paths of the V vs. j plot of Fig. 8(b).

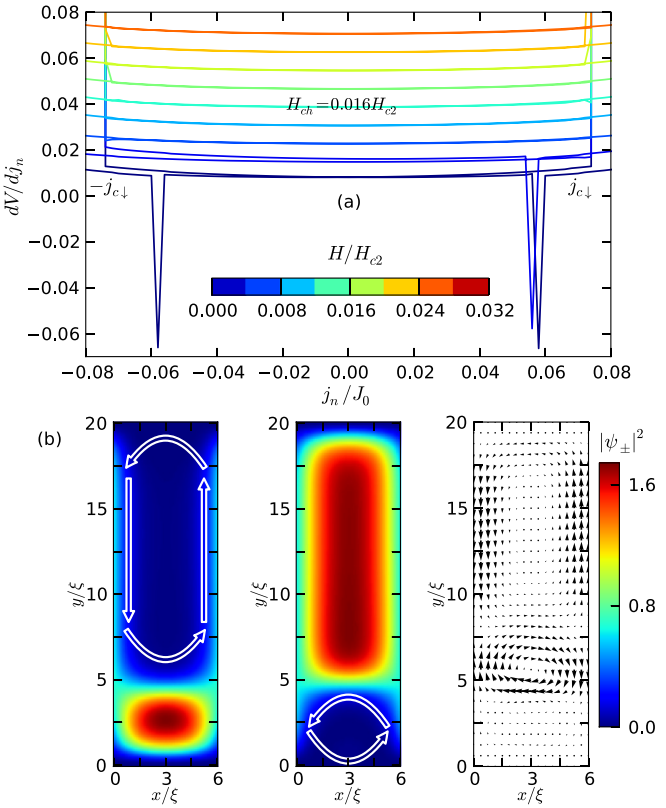

FIG. 11. (a) Differential resistivity dV/dj as a function of the applied current density j/j_0 for several values of the applied magnetic field H for the nanobridge with size $6\xi \times 20\xi$. For clarity the differential resistivities have been linearly shifted as a function of the external field H. The visible dips in the curves arise due to the discontinuities in the voltage vs current density characteristic [see top inset in Fig. 8(a)]. (b) One representative state above $H_{\rm ch}$ at zero applied current density. The displayed quantities are the same as in Fig. 9.

Fig. 8(b) for the latter case, does not reveal any hysteretic opening of the j_n-V characteristic in the superconducting phase. Thus, it is noteworthy that at zero external magnetic field hysteretic behavior can be used to distinguish monochiral states with spontaneous currents along the edges from multichiral states containing DWs.

Finally, we apply an external magnetic field perpendicular to the nanobridge of width 6ξ and report the differential resistivity dV/dj_n as a function of the applied current density j_n/j_0 for several values of applied field. In Fig. 11 the differential resistivities for different external magnetic fields H have been linearly shifted for clarity. In all curves, at the critical current densities $\pm j_{c\downarrow}$, two discontinuities are clearly seen, indicating the transition point from the normal to the superconducting phase.

It is known that degenerate states such as those of Figs. 9 and 10 split up when an external magnetic field is turned on [7]. Thus, one expects that as a consequence of the lifted degeneracy, a nonzero field H can close the hysteretic loop of the inset of Fig. 8(a). We confirm this prediction in Fig. 11(a), although we notice that the hysteretic opening survives up to some threshold field, labeled $H_{\rm ch}$. Below $H_{\rm ch}$ one can see pronounced dips in the differential resistivity, a direct consequence of the discontinuities seen in the voltage plot of Fig. 8(a) (top inset), arising due to applied current pushing the vertical DWs of Figs. 9(f) and 9(i) out of the sample and allowing the formation of the horizontal DWs of Figs. 9(c) and 9(l). Since the sample is narrow ($w_x = 6\xi$), a weak applied magnetic field is sufficient to push out the vertical DWs and favor horizontal DWs as the ground state of the system, so that the hysteretic behavior in applied current is lost.

Above $H_{\rm ch}$ in Fig. 11(a) the applied current density j_n can only stabilize one ground state, i.e., one of the two nondegenerate states, independently of the polarity of applied current. As a consequence, the hysteretic loop in the voltage vs current density characteristic is closed. In order to show the lifted degeneracy of the ground state, in Fig. 11(b) we show one representative nondegenerate state above $H_{\rm ch}$ at zero applied current. There one can see that the edge currents on one side of the DW are annihilated by the screening currents of the external magnetic field and enhanced on the other side, so that it becomes energetically favorable to displace the horizontal DW off the center (downwards in this case).

V. CONCLUSIONS

In summary, we have employed the time-dependent Ginzburg-Landau equations to study in detail chiral p-wave superconductivity in mesoscopic rectangular samples, with the goal to stabilize mono- and multichiral states in the absence of any magnetic field, as well as reveal the signatures of those states in applied electric current and magnetic field. We have reported the ground-state phase diagram of rectangular mesoscopic samples with sizes ranging from 3.5ξ

to 23ξ, where ξ is the superconducting coherence length, and classified the states according to the number of chiral domain walls they contain. The monochiral state has no domain walls but contains spontaneous currents flowing along the edges. We also noticed that the multichiral phases are made stable owing to the strong confinement, but that same confinement can overshadow the typical dipolelike magnetic field profile of the domain walls. Nevertheless, the imaging of the reported spatial profile of stray magnetic field of the multichiral states can serve as clear evidence of the time-reversal symmetry breaking in topological superconductors. Furthermore, for the same samples we reported novel features in the voltage versus current characteristics which show a hysteretic behavior in the superconducting phase when domain walls are formed due to confinement. This behavior persisted even when a weak out-of-plane magnetic field was applied, providing a useful new hallmark for indirect confirmation of the presence of domain walls in the superconducting state and thereby offering a proof of chiral p-wave superconductivity in the material of interest.

ACKNOWLEDGMENTS

This work was supported by the Research Foundation–Flanders (FWO-Vlaanderen), the COST-EU action MP1201, and the MultiSuper network.

[1] M. Z. Hasan and C. L. Kane, *Colloquium*: Topological insulators, Rev. Mod. Phys. **82**, 3045 (2010).

[2] X.-L. Qi, T. L. Hughes, S. Raghu, and S.-C. Zhang, Time-Reversal-Invariant Topological Superconductors and Superfluids in Two and Three Dimensions, Phys. Rev. Lett. **102**, 187001 (2009).

[3] B. A. Bernevig and T. L. Hughes, Time-reversal-invariant topological superconductors, in *Topological Insulators and Topological Superconductors* (Princeton University Press, Princeton, NJ, 2013), Chap. 17, pp. 214–225.

[4] A. Furusaki, M. Matsumoto, and M. Sigrist, Spontaneous Hall effect in a chiral p-wave superconductor, Phys. Rev. B **64**, 054514 (2001).

[5] M. Matsumoto and M. Sigrist, Quasiparticle states near the surface and the domain wall in a $p_x \pm i p_y$ -wave superconductor, J. Phys. Soc. Jpn. **68**, 994 (1999).

[6] J. Garaud and E. Babaev, Properties of skyrmions and multi-quanta vortices in chiral p-wave superconductors, Sci. Rep. **5**, 17540 (2015).

[7] V. Fernández Becerra, E. Sardella, F. M. Peeters, and M. V. Milošević, Vortical versus skyrmionic states in mesoscopic p-wave superconductors, Phys. Rev. B **93**, 014518 (2016).

[8] L.-F. Zhang, V. Fernández Becerra, L. Covaci, and M. V. Milošević, Electronic properties of emergent topological defects in chiral p-wave superconductivity, Phys. Rev. B **94**, 024520 (2016).

[9] P. G. Björnsson, Y. Maeno, M. E. Huber, and K. A. Moler, Scanning magnetic imaging of Sr_2RuO_4, Phys. Rev. B **72**, 012504 (2005).

[10] J. R. Kirtley, C. Kallin, C. W. Hicks, E.-A. Kim, Y. Liu, K. A. Moler, Y. Maeno, and K. D. Nelson, Upper limit on spontaneous supercurrents in Sr_2RuO_4, Phys. Rev. B **76**, 014526 (2007).

[11] C. W. Hicks, J. R. Kirtley, T. M. Lippman, N. C. Koshnick, M. E. Huber, Y. Maeno, W. M. Yuhasz, M. Brian Maple, and K. A. Moler, Limits on superconductivity-related magnetization in Sr_2RuO_4 and $PrOs_4Sb_{12}$ from scanning squid microscopy, Phys. Rev. B **81**, 214501 (2010).

[12] P. J. Curran, S. J. Bending, W. M. Desoky, A. S. Gibbs, S. L. Lee, and A. P. Mackenzie, Search for spontaneous edge currents and vortex imaging in Sr_2RuO_4 mesostructures, Phys. Rev. B **89**, 144504 (2014).

[13] Y. Maeno, T. M. Rice, and M. Sigrist, The intriguing superconductivity of strontium ruthenate, Phys. Today **54**(1), 42 (2001).

[14] A. P. Mackenzie and Y. Maeno, The superconductivity of Sr_2RuO_4 and the physics of spin-triplet pairing, Rev. Mod. Phys. **75**, 657 (2003).

[15] Y. Maeno, S. Kittaka, T. Nomura, S. Yonezawa, and K. Ishida, Evaluation of spin-triplet superconductivity in Sr_2RuO_4, J. Phys. Soc. Jpn. **81**, 011009 (2012).

[16] T. M. Rice and M Sigrist, Sr_2RuO_4: An electronic analog of ^{3}He? J. Phys. Condens. Matter **7**, L643 (1995).

[17] G. M. Luke, Y. Fudamoto, K. M. Kojima, J. Larkin, M. I. Merrin, B. Nachumi, Y. J. Uemura, Y. Maeno, Z. Q. Mao, Y. Mori, H. Nakamura, and M. Sigrist, Time-reversal symmetry-breaking superconductivity in Sr_2RuO_4, Nature (London) **394**, 558 (1998).

[18] K. D. Nelson, Z. Q. Mao, Y. Maeno, and Y. Liu, Odd-parity superconductivity in Sr_2RuO_4, Science **306**, 1151 (2004).

[19] Y. Liu, Phase-sensitive-measurement determination of odd-parity, spin-triplet superconductivity in Sr_2RuO_4, N. J. Phys. **12**, 075001 (2010).

[20] J. Xia, Y. Maeno, P. T. Beyersdorf, M. M. Fejer, and A. Kapitulnik, High Resolution Polar Kerr Effect Measurements of Sr_2RuO_4: Evidence for Broken Time-Reversal Symmetry in the Superconducting State, Phys. Rev. Lett. **97**, 167002 (2006).

[21] K. Ishida, H. Mukuda, Y. Kitaoka, K. Asayama, Z. Q. Mao, Y. Mori, and Y. Maeno, Spin-triplet superconductivity in Sr_2RuO_4 identified by ^{17}O Knight shift, Nature (London) **396**, 658 (1998).

[22] H. Murakawa, K. Ishida, K. Kitagawa, Z. Q. Mao, and Y. Maeno, Measurement of the ^{101}Ru-Knight Shift of Superconducting Sr_2RuO_4 in a Parallel Magnetic Field, Phys. Rev. Lett. **93**, 167004 (2004).

[23] S. Raghu, A. Kapitulnik, and S. A. Kivelson, Hidden Quasi-One-Dimensional Superconductivity in Sr_2RuO_4, Phys. Rev. Lett. **105**, 136401 (2010).

[24] I. A. Firmo, S. Lederer, C. Lupien, A. P. Mackenzie, J. C. Davis, and S. A. Kivelson, Evidence from tunneling spectroscopy for a quasi-one-dimensional origin of superconductivity in Sr_2RuO_4, Phys. Rev. B **88**, 134521 (2013).

[25] T. Scaffidi, J. C. Romers, and S. H. Simon, Pairing symmetry and dominant band in Sr_2RuO_4, Phys. Rev. B **89**, 220510 (2014).

[26] T. Scaffidi and S. H. Simon, Large Chern Number and Edge Currents in Sr_2RuO_4, Phys. Rev. Lett. **115**, 087003 (2015).

[27] M. Sigrist and K. Ueda, Phenomenological theory of unconventional superconductivity, Rev. Mod. Phys. **63**, 239 (1991).

[28] J.-X. Zhu, C. S. Ting, J. L. Shen, and Z. D. Wang, Ginzburg-Landau equations for layered p-wave superconductors, Phys. Rev. B **56**, 14093 (1997).

[29] W. D. Gropp, H. G. Kaper, G. K. Leaf, D. M. Levine, M. Palumbo, and V. M. Vinokur, Numerical simulation of vortex dynamics in type-II superconductors, J. Comput. Phys. **123**, 254 (1996).

[30] T. Winiecki and C. S. Adams, A fast semi-implicit finite-difference method for the TDGL equations, J. Comput. Phys. **179**, 127 (2002).

[31] M. E. Zhitomirskii, Upper critical fields and corresponding phases in superconductors with multicomponent order parameters, Zh. Eksp. Teor. Fiz. **97**, 1346 (1990) [Sov. Phys. JETP **70**, 760 (1990)].

[32] G. R. Berdiyorov, M. V. Milošević, and F. M. Peeters, Kinematic vortex-antivortex lines in strongly driven superconducting stripes, Phys. Rev. B **79**, 184506 (2009).

[33] G. R. Berdiyorov, A. K. Elmurodov, F. M. Peeters, and D. Y. Vodolazov, Finite-size effect on the resistive state in a mesoscopic type-II superconducting stripe, Phys. Rev. B **79**, 174506 (2009).

[34] M. V. Milošević and R. Geurts, The Ginzburg-Landau theory in application, Phys. C (Amsterdam, Neth.) **470**, 791 (2010).

[35] S. Lederer, W. Huang, E. Taylor, S. Raghu, and C. Kallin, Suppression of spontaneous currents in Sr_2RuO_4 by surface disorder, Phys. Rev. B **90**, 134521 (2014).

[36] W. Huang, S. Lederer, E. Taylor, and C. Kallin, Nontopological nature of the edge current in a chiral p-wave superconductor, Phys. Rev. B **91**, 094507 (2015).

[37] W. Huang, E. Taylor, and C. Kallin, Vanishing edge currents in non-p-wave topological chiral superconductors, Phys. Rev. B **90**, 224519 (2014).